05,06

Electrical properties of Sm-doped $BiFeO_3$ ceramics

© S.A. Sadykov[1,2], S.N. Kallaev[2], R.M. Emirov[1], N.M.-R. Alikhanov[1,2,¶]

[1] Dagestan State University,
Makhachkala, Russia
[2] Amirkhanov Institute of Physics, Dagestan Federal Research Center, Russian Academy of Sciences,
Makhachkala, Russia

¶ E-mail: alihanov.nariman@mail.ru

Received July 12, 2023
Revised August 27, 2023
Accepted August 29, 2023

The results of a study of the electrical properties of ceramics $Bi_{1-x}Sm_xFeO_3$ ($x = 0.05-0.20$), synthesized by the technology of spark plasma sintering of nanopowder, are presented. X-ray diffraction (XRD) showed a change in the structure of bismuth ferrite from rhombohedral to orthorhombic with increasing samarium concentration. It has been found that the substitution of samarium improves the dielectric properties of ε_r and $\tan\delta$, while the doped bismuth ferrite in the orthorhombic *Pbam* and *Pnma* phases has higher dielectric permittivity values than in the rhombohedral *R*3*c* phase. A decrease in leakage currents with increasing Sm concentration at temperatures up to 300°C was found. Near the Néel temperature, all $Bi_{1-x}Sm_xFeO_3$ compositions demonstrate a decrease in the temperature growth rate σ_{ac}. An analysis of the frequency dependence of the conductivity $\sigma_{ac}(\omega)$ at different temperatures was carried out based on the universal power law of Johnsher $\sigma \sim \omega^s$.

Keywords: $BiFeO_3$, ceramics, dielectric properties, *ac*-conductivity, crystal structure.

DOI: 10.21883/0000000000

1. Introduction

Bismuth ferrite $BiFeO_3$ (BFO) is one of the few multiferroics that simultaneously exhibits ferroelectric and (anti)ferromagnetic properties at room and higher temperatures (Curie temperature $T_C = 830$°C, Néel temperature $T_N = 370$°C) [1]. Thanks to this property BFO is potentially in demand for the creation of a new generation of electronic devices that can implement low-power control of the electric field using magnetic components [2–4]. It is known that ferroelectricity in BFO is due to the stoichiometric activity of Bi^{3+} ions, and magnetism is determined by Fe^{3+} ions. BFO has a rhombohedrally distorted perovskite structure with space group *R*3*c*. Ferroelectric polarization is oriented along [111] direction of the pseudocubic perovskite lattice cell. Magnetic moments of cations Fe^{3+} in BFO are ferromagnetically coupled in pseudocubic (111) planes and antiferromagnetically coupled between neighboring planes, forming antiferromagnetic G type ordering below Néel temperature T_N [5].

However, BFO use in devices is limited by high leakage currents and dielectric losses, which make it difficult to achieve polarization saturation and reduce the contribution of the ferroelectric phase to magnetoelectric coupling. At the synthesis stage bismuth partially volatilizes, which leads to the formation of a significant amount of oxygen vacancies and/or the formation of impurity phases, such as $Bi_2Fe_4O_9$ and $Bi_{25}FeO_{39}$. The large leakage currents and high conductivity are primarily due to the valence change from Fe^{3+} to Fe^{2+}, and the formation of oxygen vacancies to compensate for the charge. For these reasons, it is difficult to obtain pure BFO phase with stable and high electrical characteristics.

Quite a lot of studies related to the synthesis of BFO with improved dielectric properties [6–16]. One of the most common and effective ways to suppress the formation of oxygen vacancies and the appearance of secondary phases, the crystal structure stabilization by strength increasing of the ionic bond is to replace Bi^{3+} with ions of rare earth elements, such as La^{3+}, Nd^{3+}, Sm^{3+}, Ho^{3+}, Yb^{3+}, etc. [4]. Replacing Bi^{3+} with rare earth elements R with a smaller ionic radius causes a distortion of FeO_6 octahedron, change in the Fe-O-Fe angle and bond length of Bi/R-O, resulting in improved dielectric properties [8,10–12]. Doping with rare earth elements, depending on the type and degree of doping, causes structural transformations of various levels [7,12,13], which can also greatly affect the multiferroic properties of BFO.

In this paper the structure was studied and measurements of the dielectric constant, electrical conductivity and complex impedance of ceramics $Bi_{1-x}Sm_xFeO_3$ ($x = 0.05, 0.1, 0.15$ and 0.2), manufactured using spark plasma sintering technology. Ionic radius Sm^{3+} at coordination number 8 is 1.08 Å, Bi^{3+} — 1.17 Å [14]. Besides, Sm-O has a higher bond enthalpy compared to Bi-O (619 kJ/mol and 343 kJ/mol, respectively), as result the Bi^{3+} ions replacement with Sm^{3+} ions shall stabilize BFO perovskite structure, reduce the formation of oxygen vacancies and subsequently increase the dielectric constant. Previously similar studies were carried out on $Bi_{1-x}Sm_xFeO_3$ solid solutions obtained by standard solid phase synthesis [12,17,18], cold pressing of nanopowder [12], sol-gel technology [6,7,19], fast liquid-

phase sintering [20–22], and also by method of spark plasma sintering [18]. The measurement results scattering indicates the presence of certain factors responsible for changes in electrical parameters, such as sintering conditions, grain growth morphology, homogeneity, etc.

2. Objects and methods of study

The objects of the study were ceramic samples obtained from bismuth ferrite nanopowder. Nanopowders $Bi_{1-x}Sm_xFeO_3$ (BSFO) ($x = 0.05-0.20$) were synthesized by burning of organonitrate precursors obtained by evaporation of mixtures of equimolar water solutions of ferrous nitrate $Fe(NO_3)_3-9H_2O$ and bismuth nitrate $Bi(NO_3)_3-5H_2O$ with glycine. Ceramics $Bi_{1-x}Sm_xFeO_3$ was produced using the technology of spark plasma sintering of nanopowder at temperatures above 600°C in a graphite mold in air. Phase purity of samples was determined on X-ray diffractometer PANalytical Empyrean using CuK_α-radiation ($\lambda = 1.5406$ Å) in scanning range $2\theta = 5-60°$. The experimental data were processed using the HighScore Plus application program based on the PAN-ICSD diffraction database.

Dielectric constant, dielectric loss and electrical conductivity were studied using an automated setup based on LCR-78110G meter (GW Instek). The samples had the shape of a flat capacitor ~ 1 mm thick and ~ 6 mm in diameter. The density values of these samples varied in the range $\sim 7.65-7.8$ g/cm^3. The contacts were applied with silver paste followed by firing. The measurements were carried out in the frequency range 1 kHz–1 MHz in the temperature range 25–500°C with heating rate ~ 1°C/min.

3. Results and discussions

3.1. Structure study

X-ray patterns of ceramics $Bi_{1-x}Sm_xFeO_3$ (BSFO-5, BSFO-10, BSFO-15, BSFO-20) are given in Figure 1. The phase analysis showed that impurity phase are practically absent in samples (below 6% of impurity phases $Bi_2Fe_4O_9$ and $Bi_{25}FeO_{39}$). A shift of the diffraction peaks towards larger values is observed with Sm concentration increasing, this indicates lattice distortion due to the smaller ionic radius of samarium.

BSFO-5 composition crystallizes in the rhombohedral structure with space group of symmetry $R3c$. Further increase in Sm concentration results in formation of antipolar orthorhombic structure $Pbam$ (with characteristic peak $\sim 17.5°$ for $Pbam$ of bismuth ferrite structure), and sample BSFO-10 is described by two-phase model $R3c + Pbam$. For BSFO-15 sample a peak is also observed near $\sim 17.5°$, and a new (111) appears near 25.4°, it is typical for the orthorhombic structure of $SmFeO_3$ [20,21]. For ceramics BSFO-20 only peaks of the orthorhombic structure $Pnma$ are observed.

The average crystallite size calculated using the Scherrer formula is 25.6, 27, 35.3, 39.5 nm for BSFO-5, BSFO-10, BSFO-15 and BSFO-20, respectively.

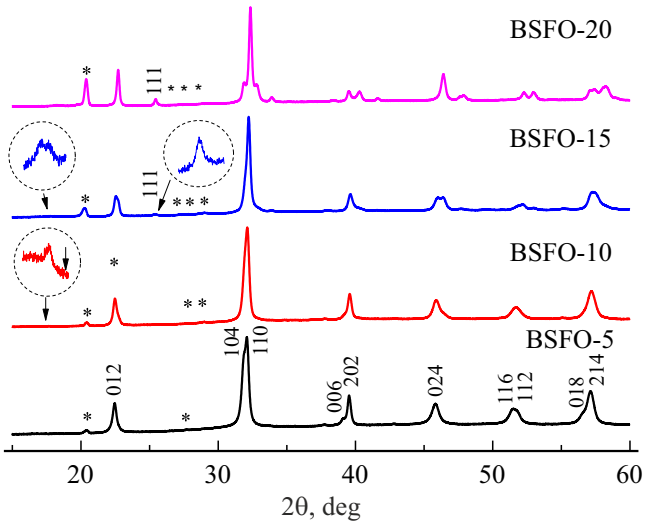

Figure 1. X-ray diffraction patterns of ceramics BSFO-5, BSFO-10, BSFO-15 and BSFO-20.

3.2. Dielectric properties

Frequency dependencies of dielectric constant (ε_r) and dielectric loss ($\tan\delta$) of samples $Bi_{1-x}Sm_xFeO_3$, measured at room temperature, are shown in Figure 2. When substitution concentration Sm^{3+} increases, the dielectric constant increases, and dielectric loss decreases. It can be seen that Sm^{3+}-modified samples demonstrate improved dielectric properties over the entire frequency range. In this case, both parameters ε_r and $\tan\delta$ exhibit frequency dependence typical for relaxors. X-ray diffraction and Raman studies shown [7,12,23] that $Bi_{1-x}Sm_xFeO_3$ samples demonstrate structural phase transition from rhombohedral (space group: $R3c$) to orthorhombic (space group: $Pnma$) cell at samarium substitution concentration about $x = 0$, 10. It was reported in papers [12,18] that during Sm doping over 10%, along with the phase $R3c$, the antipolar orthorhombic phase $Pbam$ appears. At 20% Sm the structure completely corresponds to the single-phase space group $Pnma$. This means that doped bismuth ferrite in the orthorhombic phases $Pbam$ and $Pnma$ exhibits higher dielectric properties than in the rhombohedral phase $R3c$. Since the ionic radius in Sm is smaller than that in Bi, the increase in the percentage substitution of Sm will lead to increase in the distortion of the octahedron FeO_6, change in the angle Fe^{3+}-O_2-Fe^{3+} and, accordingly, decrease in the lattice cell volume and decrease in crystallite size [8,10,14,16,21].

In the low-frequency region significant dielectric dispersion is observed, which is a common feature of polar dielectrics. At frequency of 1 kHz at room temperature the dielectric constant of BSFO-5, BSFO-10, BSFO-15 and BSFO-20 is 310, 340, 390 and 400, respectively. At frequency of 1 MHz the values of ε_r decrease to 270, 300, 335 and 360. The values ε_r given in [21] for these compositions, also synthesized by spark plasma sintering, turned out to be slightly lower (197, 217, 225 and 185, respectively).

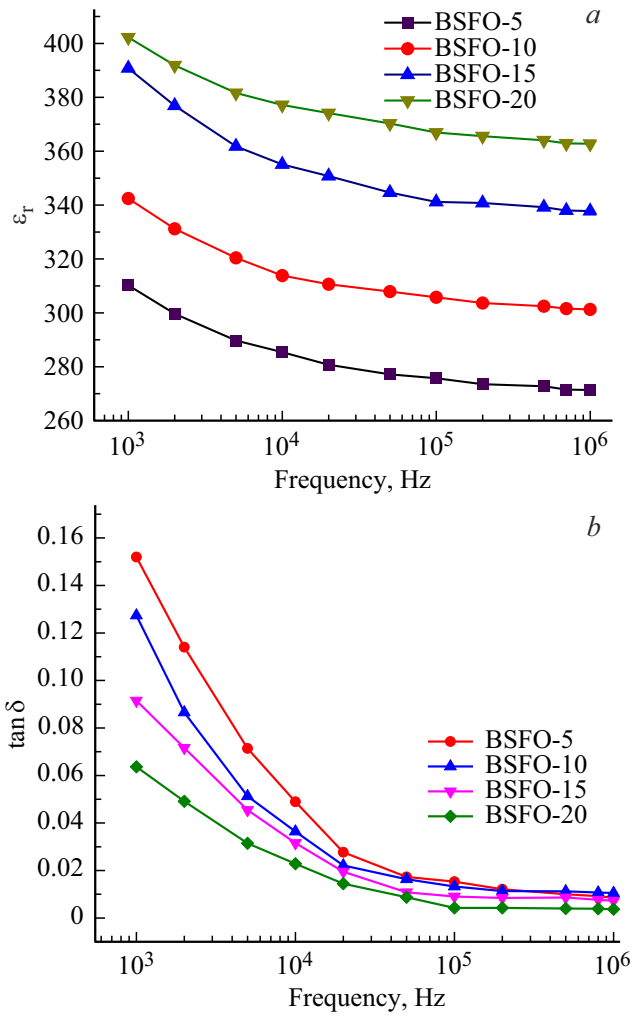

Figure 2. Frequency dependencies *a* — of dielectric constant ε_r and *b* — dielectric loss $\tan\delta$ of BSFO compositions at room temperature.

Large values of ε_r in the low-frequency region can be due to various types of polarization, such as ionic, atomic, dipole and space charge polarization (interfacial polarization). In fine-grained ceramic structures the grain boundaries represent high-resistance insulating layers between conductive grains. According to the Maxwell-Wagner model of interfacial polarization, charges accumulate at these boundaries and structural defects, which like dipoles in alternating electric field, cause additional local polarization and thereby increase the dielectric constant [18]. According to Koop's phenomenological theory [24], resistive grain boundaries control the dielectric constant at low frequencies, and conductive grains control at higher frequencies. In BFO-based composites the appearance of space charge is associated primarily with oxygen ion vacancies, Bi vacancies, and local charges. According to [11] oxygen vacancies arise for two reasons: due to the evaporation of Bi^{3+} ions and change in the valence state of Fe^{3+} ions, which can be described by the following equation: $2Fe^{3+} + O^{2-} \rightarrow 2Fe^{2+} + Vo^{2+} + 1/2O^{2-}$. The main reason for the higher dielectric constant in the low-frequency region can be assumed to be the dipole polarization due to the absorption of oxygen vacancies at grain boundaries, which are formed due to the multi-oxidation state of iron ions [18]. With increase in frequency, due to the inertia of relaxation processes, the contribution of dipole and interphase polarizations gradually decreases, and therefore ε_r dependence on frequency disappears. The relaxation dynamics is explained by electron hops between Fe^{2+} and Fe^{3+} at the sites of octahedra in BFO lattice and the oxygen vacancies movement over short distances at grain boundaries [7]. At higher frequencies, the electronic polarization works.

Figure 3, *a* shows temperature dependencies of dielectric constant (ε_r) and dielectric loss ($\tan\delta$) of BSFO compositions at frequency 1 kHz. As with many BFO-based multiferroics, the high temperature peaks ε_r are associated with the antiferromagnetic phase transition temperature T_N. The slight temperature shift T_N of different compositions can be correlated with change in the Fe-O-Fe angle due to structural modification when Sm^{3+} ions are replaced by Bi^{3+} ions. The main feature of Figure 3, *a* is the presence of

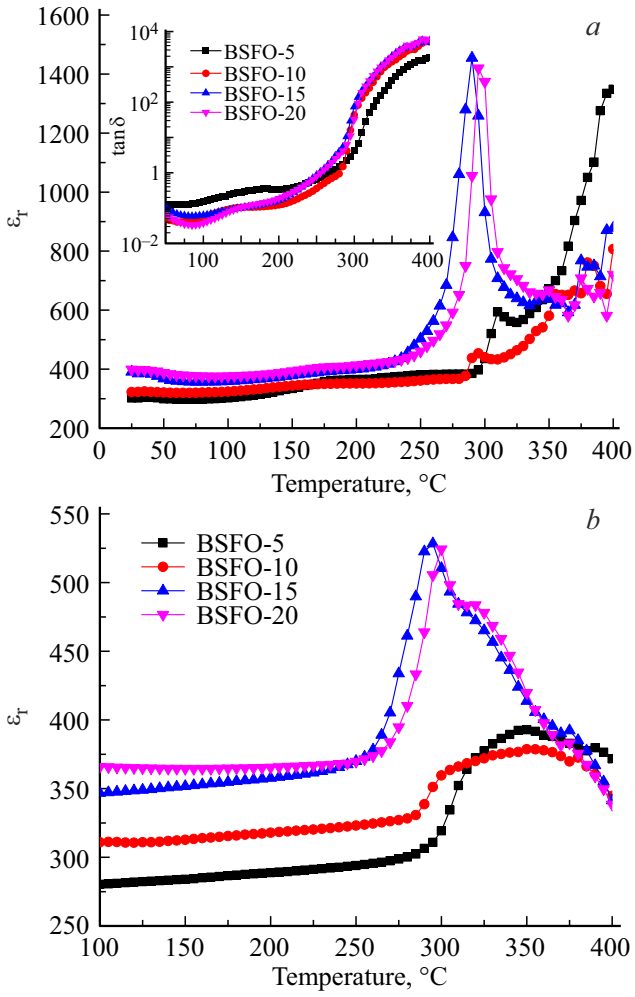

Figure 3. temperature dependencies *a* — dielectric constant ε_r, dielectric loss $\tan\delta$ (insert) of BSFO compositions at 1 kHz and *b* — temperature dependence ε_r at 100 kHz.

sharp peaks in the dependence $\varepsilon_r(T)$ near $\sim 300°C$, which are significantly larger than for the compositions BSFO-15 and BSFO-20. Anomaly in ε_r with harsh peak and harsh increase $\tan\delta$ at 300°C was also discovered For compositions BSFO-10 [19], BSFO-15 and BSFO-25 [22]. At high frequencies the peaks ε_r are suppressed (Figure 3, *b*). Consequently, the anomalies ε_r and $\tan\delta$ by their nature are not associated with structural changes and are caused by defect charges [23]. As the grain size decreases, and the area of high-resistance layers increases, an increasing number of oxygen vacancies will accumulate at the boundaries, which in alternating electric field will increase dielectric constant and conductivity [17]. A sharp increase in dielectric loss may be associated with increase in space charge polarization (localized charge) due to thermally activated process. Thus, grain boundaries are active in this temperature range.

3.3. *ac*-conductivity

Figure 4 shows graphs of temperature dependence *ac*-of conductivity (σ_{ac}) of compositions under study at frequency 1 kHz. The graph shows that σ_{ac} increases with temperature increasing, which indicates the semiconductor nature of the material's conductivity. In the temperature range $< 200°C$ (Figure 4, insert), there is a tendency for conductivity decreasing with doping level increasing. At these temperatures σ_{ac} reaches values $\sim (3-6)\cdot 10^{-8}\,\Omega^{-1}\cdot cm^{-1}$. The weak dependence of conductivity in the low-temperature region indicates a slight increase in the charged defects concentration. A sharp increase in conductivity begins at temperatures above 230°C. Near Néel temperature, σ_{ac} increases by almost five orders of magnitude ($\sim 10^{-3}\,\Omega^{-1}\cdot cm^{-1}$), indicating strong temperature activation of charge carriers. In this temperature range the opposite trend is clearly visible: increase in conductivity with doping level increasing. It can be seen that the substitution changes the nature of the curve $\sigma_{ac}(T)$, especially at higher temperatures.

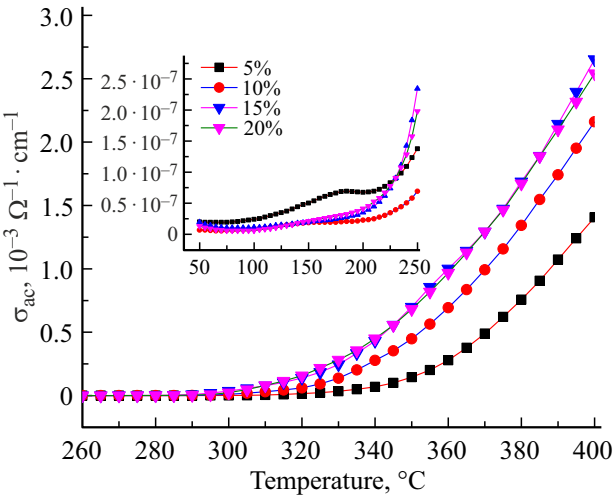

Figure 4. Temperature dependence of *ac*-conductivity of σ_{ac} BSFO ceramics, measured at a frequency of 1 kHz.

Table 1. Activation energy values for BSFO-5 ceramics

Frequency	I region	II region	III region	IV region
1 kHz	0.18	0.56	2.52	0.72
2 kHz	0.18	0.48	2.49	0.72
50 kHz	0.18	0.32	2.39	0.71
200 kHz	0.12	0.33	2.22	0.71
500 kHz	0.08	0.21	2.02	0.71
1 MHz	0.07	0.17	1.9	0.71

Table 2. Activation energy values for BSFO-10 ceramics

Frequency	I region	II region	III region	IV region
1 kHz	0.17	0.66	2.49	0.64
2 kHz	0.12	0.64	2.48	0.64
50 kHz	0.09	0.43	2.39	0.64
200 kHz	0.12	0.38	2.3	0.64
500 kHz	0.11	0.15	2.18	0.64
11 MHz	0.11	0.1	2.08	0.63

Table 3. Activation energy values for BSFO-15 ceramics

Frequency	I region	II region	III region	IV region
1 kHz	0.144	1.04	2.1	0.65
2 kHz	0.138	0.98	2.1	0.65
50 kHz	0.176	0.96	1.89	0.65
200 kHz	0.192	0.86	1.71	0.65
500 kHz	–	0.75	1.58	0.65
11 MHz	–	0.72	1.49	0.64

Table 4. Activation energy values for BSFO-20 ceramics

Frequency	I region	II region	III region	IV region
1 kHz	0.26	0.84	2.96	0.67
2 kHz	0.24	0.76	2.84	0.65
50 kHz	0.23	0.65	2.52	0.65
200 kHz	0.27	0.59	2.2	0.65
500 kHz	0.09	0.37	2	0.65
11 MHz	0.05	0.35	1.92	0.65

The nature of conductivity in different temperature ranges can be explained by changes in activation energy. With temperature increasing, the probability that charge carriers overcome the potential barriers increases, as a result of this conductivity will increase according to the exponential Arrhenius law

$$\sigma_{ac} = \sigma_0 \exp\left(-\frac{E_a}{kT}\right),$$

where E_a — energy activation, T — temperature (K), k — Boltzmann constant. The activation energy E_a can be calculated from the slope of the curves $\ln\sigma = f(1/T)$. The calculated values for BSFO ceramics are presented in Table 1–4.

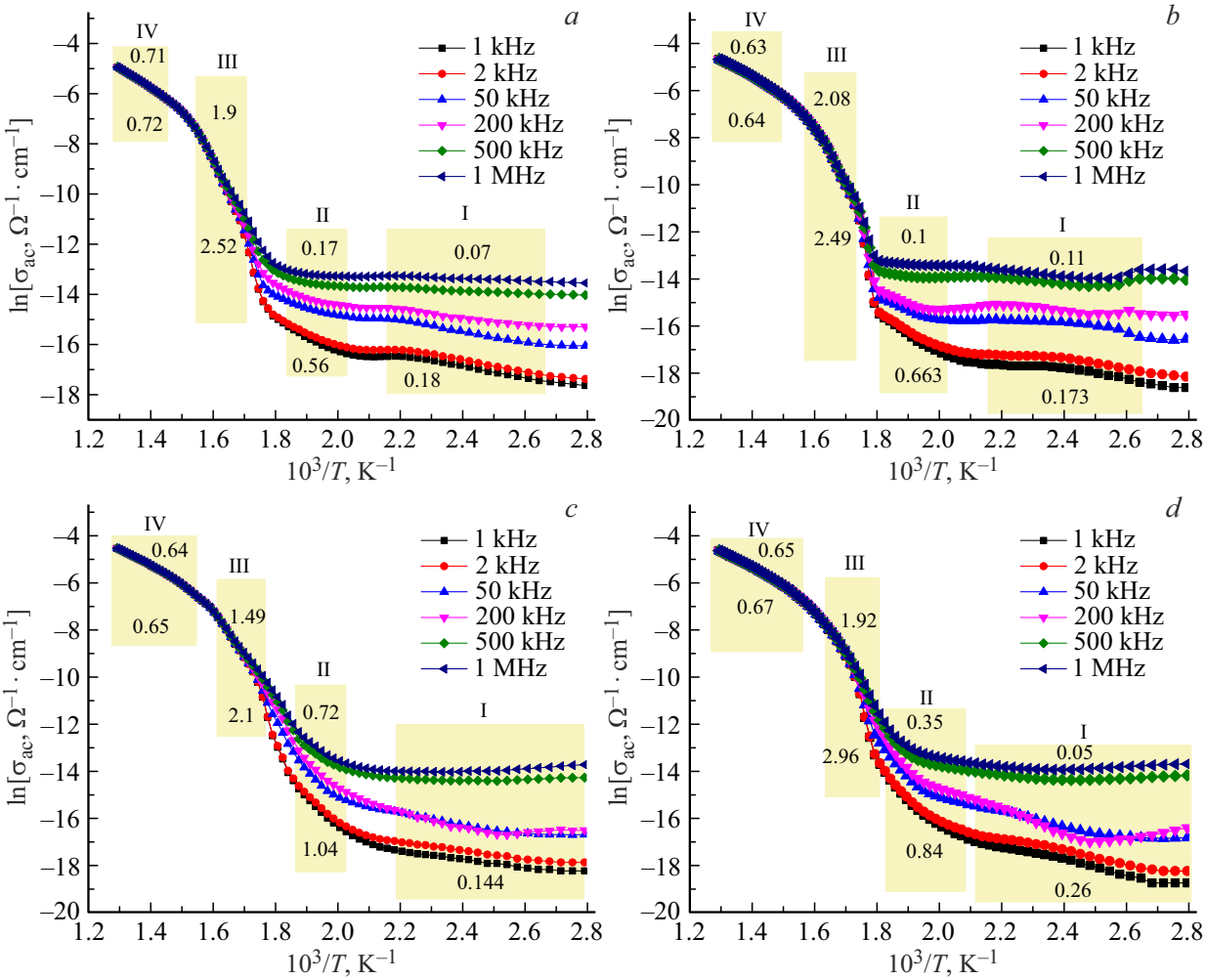

Figure 5. Change of conductivity σ_{ac} of BSFO com[ositions depending on reverse absolute temperature at some selected frequencies: *a* — BSFO-5, *b* — BSFO-10, *c* – BSFO-15, *d* — BSFO-20.

Figure 5, *a*–*c* shows change in conductivity σ_{ac} of BSFO ceramics depending on absolute temperature at some selected frequencies. It can be seen that the substitution changes the nature of the conductivity curve with temperature, especially at higher temperatures. Spectrum σ_{ac} was divided into four regions depending on slope of curves $\ln \sigma_{ac} = f(1/T)$. In different temperature regions different activation energies of alternating current electrical conductivity are observed. In the temperature range $< 230°C$ (region I), the conductivity σ_{ac} increases with frequency increasing, which indicates the frequency-dependent nature. Low values E_a in this areas ($\sim 0.2-0.05$ eV) are characteristic For electronic hopping conductivity at thermally activated superexchange interaction between ions Fe^{2+} and Fe^{3+} in octahedron FeO_6 inside grains [7]. According to the Kröger–Wink notations [9,25], the generation of oxygen vacancies and their ionization can occur in stages: $O_o^x \rightarrow V_0 \frac{1}{2} O_{2\uparrow}$; $V_0 \rightarrow V_o' + e'$; $V_o' \rightarrow V_o''' + e'$. Then electron hops across the bridge from singly ionized oxygen vacancies $Fe^{3+}-V_o'-Fe^{2+}$ will create electronic conductivity of *n*-type. Charges can only move within grains of the conducting phase, which thus become dipoles. Since electron hops between Fe^{2+} and Fe^{3+} are similar to dipole rearrangement, this process will also promote dielectric relaxation in the grains. The frequency increasing of the applied field enhances the hops of charge carriers between localized states. Accordingly, E_a decreases with frequency increasing. This means that at high frequencies less energy is required to transport charge carriers over short distances than over long distances at low frequencies.

In region II of the conductivity spectrum (230–300°C) in the frequency range of 1 kHz to 1 MHz, the activation energy varies depending on the degree of doping as follows: BSFO-5 — 0.56–0.17 eV; BSFO-10 — 0.66–0.1 eV; BSFO-15 — 1.04–0.72 eV and BSFO-20 — 0.84–0.35 eV. It can be seen that in this transition temperature range the values of E_a vary over rather wide range. It can be assumed that both the migration of singly/doubly ionized oxygen vacancies with short hop length at grain boundaries and electron hops between localized states of Fe^{2+} and Fe^{3+} ions in grains contribute to the electrical transport properties of BSFO, i.e. these values E_a indicate mixed ion-polaron

conduction mechanism. Note that E_a about 0.6 eV and higher is close to the activation energy of grain boundary relaxation [26]. It is also known that in perovskites of $BaTiO_3$ type the activation energy of singly ionized oxygen vacancies is $E_a < 0.70$ eV, and for doubly ionized oxygen vacancies the values are $E_a \sim 1.4$ eV [27].

In temperature range III (300–350°C) the dependence of activation energy E_a on doping degree of material is also observed. So, ΔE_a is 2.52–1.9 eV for BSFO-5; 2.49-2.08 eV for BSFO-10; 2.1–1.49 eV for BSFO-15 and 2.96–1.92 eV for BSFO-20. High values of E_a in this temperature range were also identified for bismuth ferrite ceramics doped with Tm (3.72–2.63 eV) [27], Dy (3.29–2.38 eV) [28], Sr (2.15 eV) [29]. The proximity of the activation energy to the optical band gap of BFO (2.04 eV) [30] suggests that upon further increase in temperature, a sharp increase in conductivity can be caused by thermal excitation of charge carriers crossing the energy gap [25,29] The significant increase in conductivity can also be affected by the coupling between moving charge carriers and magnetic moments near the Néel temperature [27].

As Figure 5 shows, all studied BSFO compositions above 350°C (region IV) are characterized by decrease in the temperature growth rate σ_{ac}. The activation energy E_a in this region at the level of 0.6–0.7 eV tends to decrease slightly with doping increasing. First of all, this is the temperature range of the antiferromagnetic phase transition, where the constants of BSFO crystal lattice change, the positions Bi^{3+} and Fe^{3+} shift when approaching the Néel temperature, and the bond angle changes between the oxygen octahedra FeO_6, which will undoubtedly lead to change in the overlap of orbitals between Fe^{3+} and O^{2-}. Structural transformations can affect not only the temperature dependence of the charge carriers concentration, but also their mobility μ. In general, the temperature dependence μ turns out to be quite complex. It should be taken into account that with temperature increasing, the optical phonons become the main mechanism of charge carriers scattering in lightly doped materials, the phonons are excited at the Debye temperature and above. In this case, the mobility μ will decrease with temperature increasing as $\sim T^{-3/2}$.

3.4. Impedance analysis

To separate the contribution of grains and grain boundaries to the electrical resistivity of polycrystalline ceramics the Nyquist plots $Z'' = f(Z')$ are plotted at different temperatures. The actual (Z') and imaginary (Z'') parts of the complex impedance $Z^* = Z' + jZ''$ can be determined from these formulas:

$$Z' = \frac{R}{1+(\omega\tau)^2}; \quad Z'' = \frac{R\omega\tau}{1+(\omega\tau)^2}, \qquad (1)$$

where $\tau = RC$ — relaxation time, ω — circular frequency.

Figure 6 shows the impedance spectra for BSFO-5 ceramics in the temperature range 25–400°C, and Figure 7

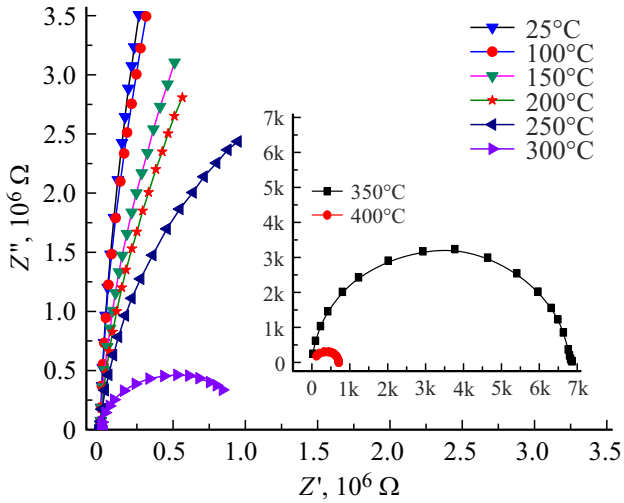

Figure 6. Spectra impedance for ceramics BSFO-5 in temperature range 25–400°C.

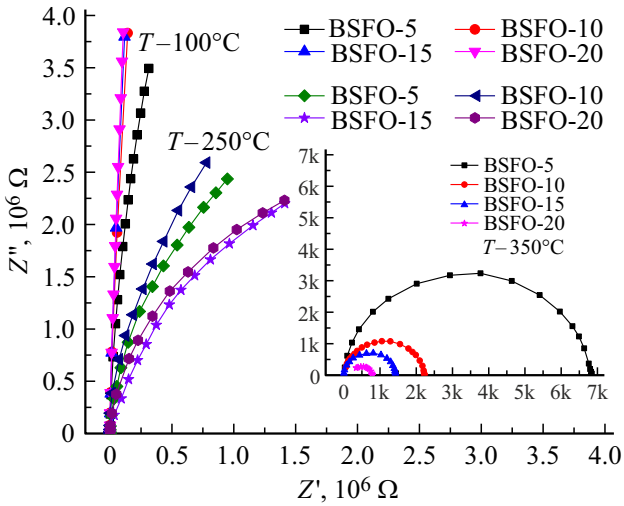

Figure 7. Comparison of impedance spectra for BSFO ceramics at fixed temperatures.

shows for comparison the impedance diagrams for all compositions at fixed temperatures. In Figure 6 three regions are distinguished: the first region corresponds to the temperature range below 250°C and describes the dielectric behavior with high resistivity, the second region is observed at temperature about 250°C, and the third region — at temperatures of 350°C and above with extremely low resistivity of the components. It can be seen that the diameters of the semicircles decrease with temperature increasing, exhibiting semiconducting behavior. At the same time, below 250°C the graphs of the complex impedance of the samples do not have the shape of full semicircle, which makes it difficult to approximate them in the frequency domain with simple equivalent circuits. However, one can point to the contribution of the sample grain in the high-frequency region and the grain boundaries in the low-frequency region.

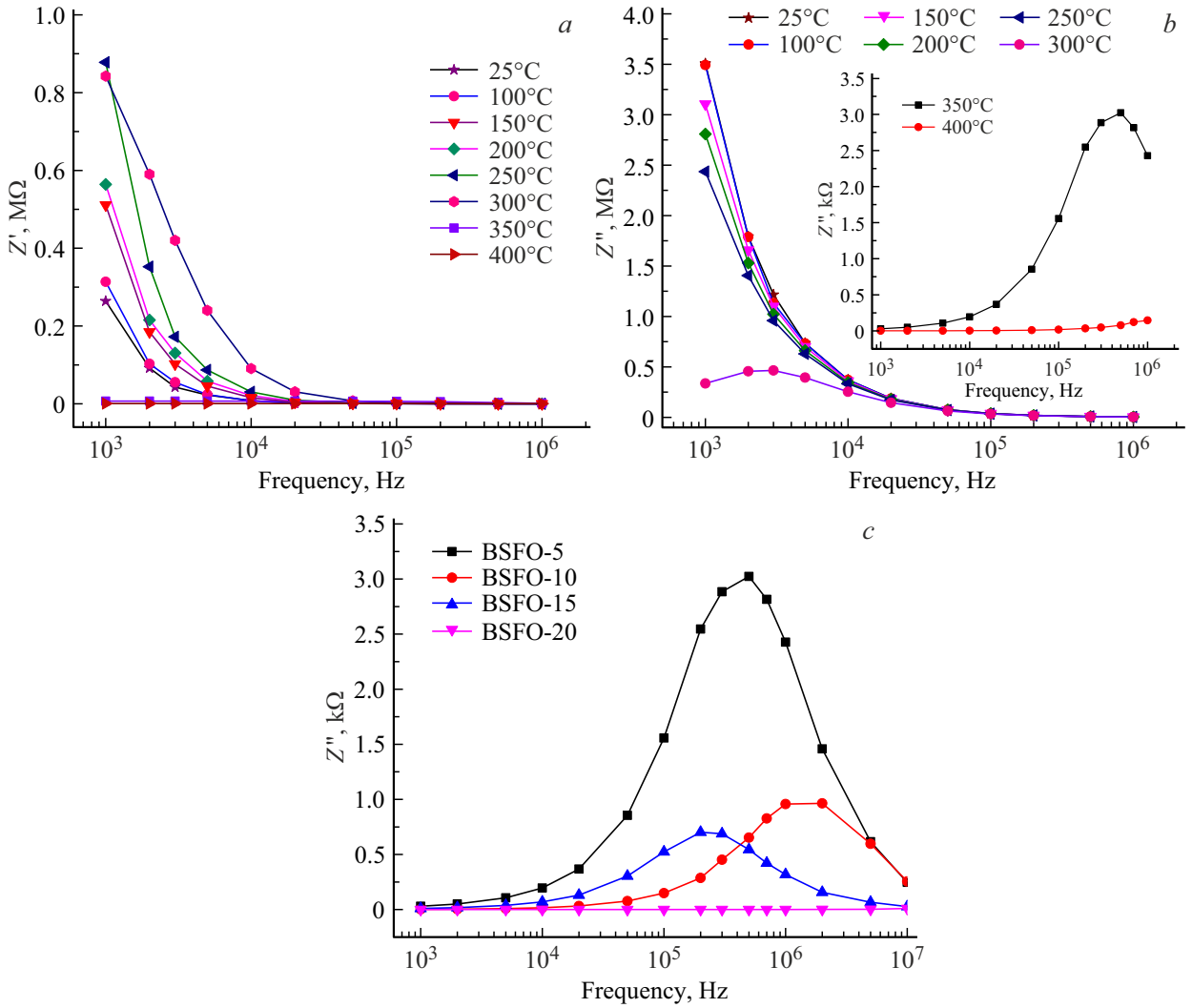

Figure 8. Frequency changes *a* — actual 97xE, *b* — imaginary Z' of part of comprehensive impedance for BSFO-5 at various selected temperatures, *c* — comparison parameter impedance Z' of BSFO samples at 350°C.

The impedance graphs of the samples at high temperatures consist of depressed semicircular arcs, indicating the possibility of more than one relaxation in the sample. The centers of the arcs also locate below the actual axis Z', which indicates the presence of non-Debye type relaxation in the samples. This behavior is usually attributed to several factors [31] such as grain orientation, grain boundaries, stress-strain state, and defect distribution. The observed decrease in the size of semicircular arcs with Sm doping increasing at temperature of 350°C and above indicates decrease in the resistance in the samples (Figure 7). The numerical values of resistance R at low frequencies, estimated from the points of intersection of semicircular arcs with the axis Z', are about kΩ. The appearance of a single semicircular arc confirms the dominance of one conduction mechanism in given temperature range. This gives reason to believe that the electrical parameters do not depend on grain boundaries, and the conductivity of the sample is volumetric effect. This also means that there are no additional contributions to conductivity along intercrystalline boundaries, which is typical for ceramic materials. Therefore, relaxation in the spectrum can only be represented by a simple equivalent circuit with *RC*-circuit.

Figure 8, *a, b* shows the frequency changes in the actual and imaginary parts of the impedance at various selected temperatures for BSFO-5 composition. One can see decrease in Z' at all temperatures with frequency increasing. The merging of the spectrum Z' at high frequencies (above 10 kHz) is a consequence of the space charge release due to the decreasing of potential barriers [25,28]. With temperature increasing Z' decreases, providing negative temperature coefficient of resistance in the relaxation region. This trend was found for all BSFO ceramics.

The loss spectrum (Z') has a number of important features. The imaginary part of the impedance Z'' also relaxes in the low-frequency region. However, at temperatures of 300°C and above, frequency-dependent asymmetric peaks appear, indicating stronger relaxation at higher tempera-

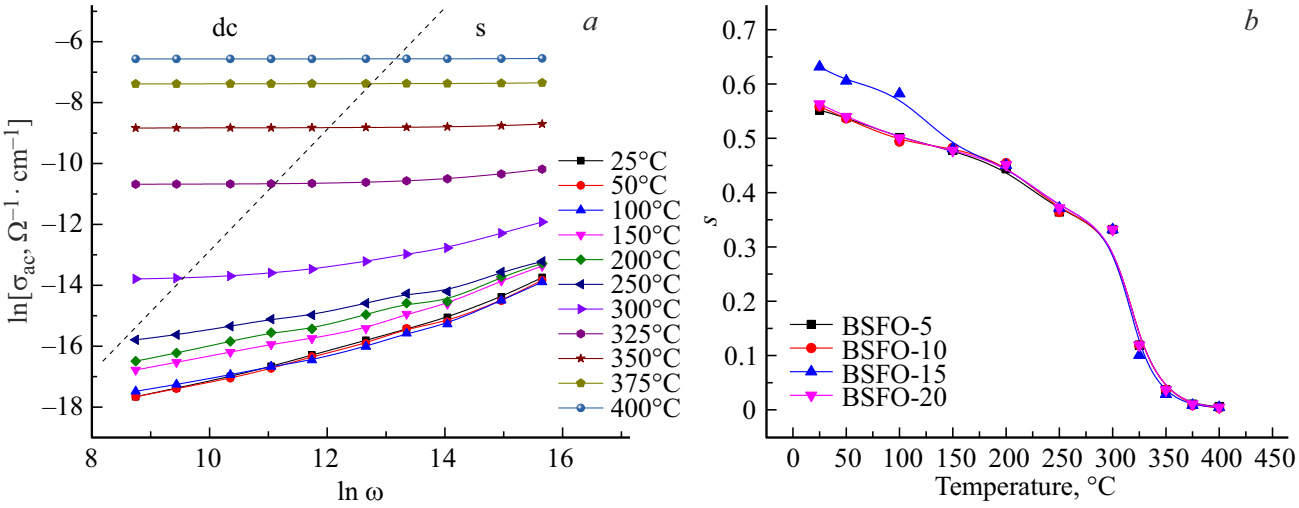

Figure 9. *a* — frequency dependences of conductivity $\sigma_{ac}(\omega)$ at different temperatures for BSFO-5 composition; *b* — decrease in exponent s with temperature increasing according to the correlated barrier hops (CBH) model.

tures. Relaxation peaks appear when the hopping frequency of localized electrons becomes approximately equal to frequency of the applied field. The asymmetric broadening of the peaks with temperature increasing indicates the presence of electrical relaxation process in the sample under the influence of temperature [28]. With temperature increasing, the position of the peak Z'' shifts towards higher frequencies. Thus, with temperature increasing from 300 to 400°C, the resonant frequency corresponding to Z'_{max} shifts from the kilohertz range to the megahertz range. So, at high temperatures and frequencies the space charge requires less time to relax. This behavior of the impedance spectrum indicates the change in the temperature-dependent mechanism of charge carrier transport in the material.

Figure 8, *c* shows the comparison of the impedance parameter Z'' of the studied compositions at 350°C. There is a trend for the peaks shift with degree of Sm doping increasing towards higher frequencies, as well as a noticeable decrease in the value Z''_{max}.

3.5. Frequency dependence σ_{ac}

Figure 9, *a* shows the frequency dependences of conductivity $\sigma_{ac}(\omega)$ at different temperatures for BSFO-5 composition. The graphs of the frequency dependences of conductivity of other studied compositions are similar to those presented in Figure 9. The dependences $\sigma_{ac}(\omega)$ are characterized by i) dispersion of conductivity spectra at low frequencies and their narrowing at high frequencies, respectively, with temperature increasing; ii) the appearance of frequency-dependent plateau above 300°C, the plateau expansion into the high-frequency region with temperature increasing.

To study the frequency behavior of conductivity in disordered structures at fixed temperature, it is convenient to use the power relation proposed by Jonsher [32]:

$$\sigma_{ac} = \sigma_0 + A\omega^s, \tag{2}$$

where σ_0 — frequency-dependent part of conductivity (or dc-conductivity), coefficient A and exponent s — constants dependent on internal properties and temperature of material. Term $A\omega^s$ characterizes the dispersion phenomena of frequency dependence of conductivity, where exponent s is limited by values $0 < s < 1$. The frequency exponential function $\sigma(\omega)$ indicates the hopping nature of conductivity. The values of the frequency exponent are determined by the slopes of the dependence curves $\ln\sigma_{ac}$ on $\ln\omega$ in the frequency range, as shown in Figure 9, *a*.

At low frequencies a frequency-independent region is identified, where translational hops of charge carriers over long distances for a long time create dc-conductivity. This region is followed by the dispersion region. The indicator s ($0 < s < 0.7$) characterizes the frequency region in which the hop-like transfer of charge carriers over short distances (electrons in grains and oxygen vacancies along grain boundaries) dominates. The values of the exponent s decrease with temperature increasing (Figure 9, *b* and tend to zero at higher temperatures (> 350°C). This indicates the presence of dc conductivity at high temperatures also in the high frequency range.

This behavior of $s(T)$ in equation (2) is associated with the hopping mechanism in the correlated barrier hop (CBH) model for ac-conductivity, developed by Elliot [33] for simultaneous two-electron hopping over the Coulomb barrier W_M separating two defect centers. According to the CBH model the exponent s should decrease with temperature increasing, this is observed in our studies. In this model the frequency exponent s is expressed by the following relation:

$$s = 1 - \frac{6kT}{W_M + kT\ln(\omega\tau_0)}, \tag{3}$$

where W_M — maximum barrier height (W_M is defined as the energy required to move charge carrier from one site to another), τ_0 — effective relaxation time, which is as large as vibration period of atoms ($\tau_0 = 10^{-13}$ s). To a first approximation (3) gives a simple expression for the frequency index s:

$$s = 1 - \frac{6kT}{W_M}. \quad (4)$$

From (4) it follows that W_M decreases with temperature increasing, which corresponds to decrease in the exponent s. This will lead to increase in the number of free charge carriers that can hop over the barrier, and, consequently, to increase in conductivity. The bond energy of carriers in their localized states W_M, determined from the temperature dependence of the exponent s for BSFO-5 composition at temperatures 300, 350 and 400°C was 0.44, 0.33 and 0.07 eV, respectively. A sharp drop in WM values near the Néel temperature T_N leads to change in the conductivity mechanism with the ac-conductivity transformation into dc-conductivity in grains.

4. Conclusion

We studied the structure, dielectric properties and electrical conductivity of ceramics $Bi_{1-x}Sm_xFeO_3$ ($x = 0$; 0.05; 0.1; 0.15; 0.2), obtained using the technology of spark plasma sintering of nanopowder. X-ray diffraction showed the formation of orthorhombic phase $Pbam$ in composition with $x = 0.1$, along with the rhombohedral phase $R3c$. It was established that samarium replacement improves the dielectric properties ε_r and $\tan\delta$, and bismuth-doped ferrite in the orthorhombic phases $Pbam$ and $Pnma$ has more higher dielectric constant values than in the rhombohedral phase $R3c$. The decrease in leakage currents was detected with Sm concentration increasing at temperatures up to 300°C. Based on the analysis of Nyquist plots and frequency-temperature dependences of impedance, the non-Debye type of relaxation process in the samples was identified. Analysis of the frequency dependence of conductivity $\sigma_{ac}(\omega)$ at different temperatures was carried out on the basis of Jonsher universal power law $\sigma \sim \omega^s$. It was shown that with temperature increasing the exponent s decreases and at high temperatures > 350°C tends to zero. This behavior of $s(T)$ is associated with the hopping mechanism in the correlated barrier hops (CBH) model.

Acknowledgments

The authors are grateful to M.R. Dzhamaludinov for help in solving technological issues.

Funding

This study was funded by the Russian Science Foundation (RSF) under project No. 23-22-00130.

Conflict of interest

The authors declare that they have no conflict of interest.

References

[1] J. Wang, J.B. Neaton, H. Zheng, V. Nagarajan, S.B. Ogale, B. Liu, D. Viehland, V. Vaithyanathan, D.G. Schlom, U.V. Waghmare, N.A. Spaldin, K.M. Rabe, M. Wuttig, R. Ramesh. Science **299**, 1719 (2003).
[2] S.M. Yakout. J. Supercond. Nov. Magn. **342**, *34*, 317 (2021).
[3] N.A. Spaldin, R. Ramesh. Nat. Mater. **183**, *18*, 203 (2019).
[4] J. Wu, Z. Fan, D. Xiao, J. Zhu, J. Wang. Prog. Mater. Sci. **84**, 335 (2016).
[5] C. Ederer, N.A. Spaldin. Phys. Rev. B: Condens. Matter Mater. Phys. **71**, 1 (2005).
[6] Y.B. Yao, W.C. Liu, C.L. Mak. J. Alloys Compd. **527**, 157 (2012).
[7] B. Deka, S. Ravi, D. Pamu. Ceram. Int. **43**, 16580 (2017).
[8] T. Durga Rao, A. Kumari, M.K. Niranjan, S. Asthana. Phys. B Condens. Matter. **448**, 267 (2014).
[9] J. Kolte, P.H. Salame, A.S. Daryapurkar, P. Gopalan. AIP Adv. **5**, 097164 (2015).
[10] Z. Yan, K.F. Wang, J.F. Qu, Y. Wang, Z.T. Song, S.L. Feng. Appl. Phys. Lett. **91**, 082906 (2007).
[11] J.P. Liu, Z.L. Lv, Y.X. Hou, L.P. Zhang, J.P. Cao, H.W. Wang, W.B. Zhao, C. Zhang, Y. Bai, K.K. Meng, X.G. Xu, J. Miao. Ceram. Int. **48**, 17328 (2022).
[12] S.A. Sadykov, N.M.R. Alikhanov, S.N. Kallaev, M.K. Rabadanov, D.K. Palchaev, Z.K. Murlieva, R.M. Emirov. Phys. Solid State. **61**, 2069 (2019).
[13] D.V. Karpinsky, I.O. Troyanchuk, M. Tovar, V. Sikolenko, V. Efimov, A.L. Kholkin. J. Alloys Compd. **555**, 101 (2013).
[14] R.D. Shannon. Acta Crystallogr. Sect. A **32**, 751 (1976).
[15] E. Palaimiene, J. Macutkevic, D.V. Karpinsky, A.L. Kholkin, J. Banys. Appl. Phys. Lett. **106**, 012906 (2015).
[16] S. Pattanayak, R.N.P. Choudhary, P.R. Das. Electron. Mater. Lett. **10**, 165 (2014).
[17] H. Dai, Z. Chen, T. Li, Y. Li. J. Rare Earths. **30**, 1123 (2012).
[18] S.G. Nair, J. Satapathy, N.P. Kumar. J. Alloys Compd. **895**, 162599 (2022).
[19] D.V. Karpinsky, I.O. Troyanchuk, A.L. Zheludkevich, O.V. Ignatenko, M.V. Silibin, V.V. Sikolenko. Phys. Solid State. **58**, 1590 (2016).
[20] L. Li, H. Qin, L. Zhang, J. Hu. RSC Adv. **6**, 60967 (2016).
[21] T. Wang, X.L. Wang, S.H. Song, Q. Ma. Ceram. Int. **46**, 15228 (2020).
[22] F. Zhang, X. Zeng, D. Bi, K. Guo, Y. Yao, S. Lu. Mater. **11**, 2208 (2018).
[23] H. Singh, K.L. Yadav. Ceram. Int. **41**, 9285 (2015).
[24] C.G. Koops. Phys. Rev. **83**, *1*, 121 (1951).
[25] K. Auromun, R.N.P. Choudhary. Ceram. Int. **45**, 20762 (2019).
[26] A.R. Makhdoom, M.J. Akhtar, R.T.A. Khan, M.A. Rafiq, M.M. Hasan, F. Sher, A.N. Fitch. Mater. Chem. Phys. **143**, 256 (2013).

[27] S. Kumari, N. Ortega, A. Kumar, S.P. Pavunny, J.W. Hubbard, C. Rinaldi, G. Srinivasan, J.F. Scott, R.S. Katiyar. J. Appl. Phys. **117**, 114102 (2015).
[28] L. Thansanga, A. Shukla, N. Kumar, R.N.P. Choudhary. J. Mater. Sci. Mater. Electron. **32**, 21337 (2021).
[29] B. Kaur, L. Singh, V.A. Reddy, D.-Y. Jeong, N. Dabra, J.S. Hundal. Int. J. Electrochem. Sci. **11**, 4120 (2016).
[30] N.M.R. Alikhanov, M.K. Rabadanov, F.F. Orudzhev, S.K. Gadzhimagomedov, R.M. Emirov, S.A. Sadykov, S.N. Kallaev, S.M. Ramazanov, K.G. Abdulvakhidov, D. Sobola. J. Mater. Sci. Mater. Electron. **32**, 13323 (2021).
[31] A.K. Roy, K. Prasad, A. Prasad. ISRN Ceram. 1–12 (2013).
[32] A.K. Jonscher. Nature **267**, 673 (1977).
[33] S.R. Elliott. Adv. Phys. **36**, 135 (1987).

Translated by I.Mazurov